Research Square

Preprints are preliminary reports that have not undergone peer review.
They should not be considered conclusive, used to inform clinical practice,
or referenced by the media as validated information.

Green Laser-Induced Graphene from Avocado Seed Waste: Process Optimization and Structural Defect Control

Byron Tipán
Universidad Yachay Tech
Gema González
ggonzalez@yachaytech.edu.ec

Universidad Yachay Tech
Carlos Reinoso
Universidad Yachay Tech
Fernando Pantoja
National Polytechnic School

Research Article

Keywords: Laser-induced graphene, avocado seed, green synthesis, synthesis optimization

Posted Date: June 17th, 2026

DOI: https://doi.org/10.21203/rs.3.rs-9847865/v1

License: This work is licensed under a Creative Commons Attribution 4.0 International License.
Read Full License

Additional Declarations: No competing interests reported.

Version of Record: A version of this preprint was published at Lasers in Manufacturing and Materials Processing on October 15th, 2026. See the published version at https://doi.org/10.1007/s40516-026-00373-5.

Green Laser-Induced Graphene from Avocado Seed Waste: Process Optimization and Structural Defect Control

Byron Tipán[1-2], Gema González[1], Carlos Reinoso[1], Fernando Pantoja[2]

[1] Yachay Tech University, School of Physical Sciences and Nanotechnology, 100119 Urcuquí, Ecuador

[2] Departamento de Materiales, Facultad de Ingeniería Mecánica, Escuela Politécnica Nacional, Ladrón de Guevara, E11-253 Quito, Ecuador

Email: btipan@yachaytech.edu.ec

Abstract

Laser-induced graphene (LIG) has emerged as a versatile method for producing porous, conductive graphitic structures from carbon-rich precursors. In this work, an unconventional and sustainable precursor—Fuerte avocado seed (Persea americana Mill) waste—was explored for the green synthesis of LIG via CO_2 laser engraving. Avocado seed powder was processed into compact pellets and systematically irradiated under varying synthesis parameters, including laser power, scan speed, irradiation area, number of passes, and processing atmosphere.

The analysis of these variables is essential to understand LIG formation, as laser energy directly influences carbon reorganization during irradiation. Additionally, the precursor composition strongly affects its graphitization behavior. Unlike many studies that require flame retardants, the optimized synthesis conditions and a suitable avocado seed powder size enabled successful LIG formation without flame retardants.

A total of 5 samples were then prepared for irradiation in a rectangular geometry measuring 10 × 5 mm, thereby controlling the irradiation area to 50 mm^2. Raman spectroscopy was used to analyze the degree of graphitization of the material, yielding LIG with a low defect density, as indicated by an I_D/I_G ratio of 0.16 ± 0.07 cm^{-1}. Furthermore, SEM images revealed a characteristic porous morphology of this material, and a sheet resistance of 25.31 ± 1.09 Ω sq^{-1} was observed.

These results show that a manufacturing process for pellets without flame retardants can yield satisfactory results for materials such as LIG. This study demonstrates that avocado seed biomass is a viable and low-cost precursor for LIG production and underscores the

importance of optimizing process parameters to control structural defects and chemical functionality in sustainable graphene materials.

Keywords: Laser-induced graphene, avocado seed, green synthesis, synthesis optimization.

1. Introduction

Graphene is a two-dimensional nanomaterial composed of sp^2-hybridized carbon atoms arranged in a hexagonal lattice. The strong σ-bonds provide structural stability, while the delocalized π-electron system confers exceptional electrical and thermal conductivity. [1] Due to its remarkable Young's modulus (~1100 GPa), high thermal conductivity (~5000 $W\ m^{-1}\ K^{-1}$), and outstanding charge carrier mobility (~200,000 $cm^2\ V^{-1}\ s^{-1}$), graphene has attracted significant interest across physics, materials science, and engineering. [2]

However, individual graphene sheets tend to restack via van der Waals interactions, forming graphite-like structures and thereby limiting the accessible surface area. To overcome this limitation, considerable research has focused on developing three-dimensional (3D) graphene architectures. [3] These structures, typically consisting of interconnected few-layer graphene domains, preserve many of graphene's intrinsic properties while introducing macroscopic porosity and enhanced mechanical stability. [4]

A breakthrough in scalable graphene fabrication was the development of laser-induced graphene (LIG), first reported by Ye et al. in 2014. [5] In this process, a CO_2 laser converts carbon-rich precursors into porous graphene through rapid photothermal pyrolysis. The extremely short heating and cooling times promote kinetic carbonization, often referred to as "kinetic graphene," in which graphitic domains form before full structural reorganization into crystalline graphite. [5]

Laser power is a crucial factor in driving the structural transformation of precursor materials into laser-induced graphene, as it helps break bonds and rearrange atoms during graphitization. Scan speed affects heat buildup in nearby areas, thereby raising the material's temperature. In the case of laser-induced graphene, laser defocusing—which increases the spot size—is vital for effective graphitization of the precursor. Finally, the choice of processing atmosphere greatly affects the surface properties of the final

material, enabling the formation of hydrophobic surfaces under argon and hydrophilic surfaces in the absence of inert gases. [6], [7]

Commercial infrared laser systems ($\lambda \approx 10.6$ μm) provide a cost-effective and accessible route for LIG fabrication. [8] Polyimide (PI) has been widely used as a precursor due to its high aromatic carbon content, which favors graphitic rearrangement during laser irradiation. [9] Raman spectra of PI-derived LIG typically display a prominent 2D band near 2700 cm^{-1}, characteristic of few-layer graphene, along with I_D/I_G ratios indicative of partial structural disorder. [10]

Beyond synthetic polymers, increasing attention has been directed toward sustainable and bio-derived carbon sources. Green synthesis strategies aim to replace petroleum-based precursors with renewable or waste-derived biomass, aligning advanced nanomaterial production with circular economy principles. [11], [12] Various food and agricultural wastes—including orange peel, almond shells, pomelo peel, and treated paper—have recently been demonstrated as promising LIG precursors. [13], [14], [15], [16]

Avocado seeds constitute an abundant and largely underutilized agro-industrial by-product. In the case of the *Fuerte* variety (*Persea americana* Mill.), which is widely cultivated in Ecuador, the seed represents approximately 25–30% of the total fruit mass. It is typically discarded after processing and consumption. From a materials perspective, avocado seeds are rich in carbonaceous biopolymers, including lignin, cellulose, and hemicellulose, which serve as effective precursors for thermally derived carbon materials. [17], [18], [19]

In lignocellulosic and cellulosic precursors, graphitization poses significant challenges due to the predominance of aliphatic carbon structures and their low thermal resistance. To address these limitations, approaches such as incorporating flame retardants—enhancing the material's thermal stability—and using ultrashort-pulse lasers, which enable more controlled conversion with reduced thermal degradation, have been explored. Recent studies have also demonstrated the feasibility of producing LIG on these substrates using CO_2 lasers, underscoring the need for further investigation into laser–material interactions in precursors with diverse compositions and physicochemical properties. [20], [21]

During the conversion into graphene structures, laser irradiation induces the cleavage of chemical bonds such as C–C, C–O, and C–H, followed by the reorganization of carbon into graphite-like structures. Photochemical degradation studies have shown that certain bonds are more susceptible to cleavage, whereas the central aromatic framework tends to be preserved, facilitating its subsequent rearrangement. However, photochemical processes alone are insufficient to achieve graphitization. Pyrolytic processes are required to remove undesired structures and promote the formation of more aromatic carbon networks. These processes occur on extremely short timescales and can be described in two main stages: (i) bond cleavage induced by combined photochemical and thermal effects, leading to the release of volatile species; and (ii) the rearrangement of aromatic structures into graphitic networks dominated by sp^2-hybridized carbon. [22]

In this context, it is important to note that, beyond demonstrating laser-induced graphitization in biomass precursors, a key challenge remains establishing a reproducible and physically meaningful optimization framework. In lignocellulosic systems, the interplay between thermal stability, volatile release, and carbon reorganization introduces competing effects that cannot be captured by a single metric. Therefore, defining an operational processing window requires a multi-criteria approach that simultaneously considers defect density, structural integrity, and process stability. This work addresses this gap by proposing a systematic correlation between laser parameters, thermal gradients, and the resulting graphitic structure, enabling a more rigorous definition of optimal processing conditions for heterogeneous biomass-derived precursors.

2. Experimental

2.1. Analysis of parameters for irradiation

2.1.1. Pellet fabrication

Fuerte avocado seeds were obtained as by-products from the food industry, thoroughly washed with distilled water, dried, and mechanically cut into smaller fragments. The material was subsequently oven-dried at 60 °C to remove residual moisture, then ground into a fine powder. The powder was sieved using standard mesh sizes to obtain fractions with different particle-size distributions, which were then evaluated for their influence on laser-induced graphene (LIG) formation. The sieved fractions were stored in airtight containers to prevent moisture uptake. Three particle-size fractions corresponding to sieve mesh numbers 80, 140, and 270 were selected for further study and labeled T-80, T-140,

and T-270, respectively, to facilitate experimental design. Compact pellets of 500.0 ± 0.1 mg were fabricated from each powder fraction using a manual hydraulic press with a pressure of 25 MPa. The diameter and thickness were 22.0 ± 0.3 and 1.34 ± 0.01 mm, respectively.

2.1.2. Parameter optimization

LIG synthesis was optimized through four sequential experimental stages designed to determine the most suitable processing conditions. The parameters investigated are summarized in Table 1. The selected geometry was a 2 mm square on each side to control the irradiation area, enabling a consistent comparison between the samples. Laser power (maximum output 80 W) and scanning speed — defined as the linear velocity of the laser beam during patterning — were systematically varied. The number of lasers that pass over the same region was also evaluated as an additional processing parameter. To assess the effect of the processing, the laser system's standard air-assist flow was replaced with a controlled argon flow in selected experiments. At the end of the study on the optimization of synthesis parameters, a total of 18 samples were prepared at 20 °C and 50 % relative humidity.

Table 1. Laser processing parameters used for LIG synthesis from avocado seed pellets.

	Number of samples	**N° Sieve**	**Irradiation area**	**Scanning speed**	**Laser power**	**Argon flow**	**Number of passes**	**Cooling time**	**Line spacing**	**Defocus distance**	**Spot size**
			[mm^2]	[mm s^{-1}]	[%]	[L/min]		[min]	[mm]	[mm]	[mm]
1	2	T-80	4	60	10	-	2	1	0.02	13.4	0.72
							2	0			
2	3	T-80	4	50	10	-	1	-	0.02	13.4	0.72
				65	11						
				65	12						
3	4	T-80	4	55	10	5	1	-	0.02	13.4	0.72
				50							
				45							
				40							
4	3	T-80	1	50	10	5	1	-	0.02	13.4	0.72
			4								
			9								
	3	T - 140	1	50	10	5	1	-	0.02	13.4	0.72
			4								
			9								
	3	T - 270	1	50	10	5	1	-	0.02	13.4	0.72
			4								

			9								

2.1.3. Characterization

Raman characterization was performed using a HORIBA SCIENTIFIC LabRAM HR Evolution spectrophotometer with a 532 nm monochromatic beam and a laser power of 3.2%. Measurements were taken at each synthesis stage to optimize the quality of the resulting LIG. In the final stages of optimization, analyses are performed at three points to compare results. For X-ray photoelectron spectroscopy (XPS), a PHYSICAL ELECTRONICS VERSAPROBE PHI 5000 instrument with a Ka aluminum source was used. To better understand the spectra obtained by these two techniques, the peaks in each spectrum were deconvolved using OriginPro data analysis and graphing software. Fourier transform infrared spectroscopy (FTIR) was conducted using a JASCO FT/IR-4700 instrument with a standard light source.

2.2. Optimal Procession parameters of LIG

2.2.1. Pallet fabrication and synthesis of LIG

The pellet preparation process was the same as described in Section 2.1.1. The geometry for the final LIG synthesis was a 10 × 5 mm rectangle with an irradiation area of 56.4 ± 3 mm^2, applied to 5 different pellets. The synthesis parameters were as follows: T-80 particle size was used, and a single irradiation was performed with a laser power of 11% at a speed of 50 mm s^{-1}, a defocus distance of 9 mm, and a line spacing of 0.02 mm. The preparation was performed at 20 °C and 50 % relative humidity.

2.2.2. Characterization

Raman characterization was performed using a HORIBA SCIENTIFIC LabRAM HR Evolution spectrophotometer with a 532 nm monochromatic beam and a laser power of 3.2%. Measurements were performed at three points of each pellet to compare results. SEM micrographs were obtained using the LMU model scanning electron microscope with a tungsten filament, achieving vacuum levels of 8.5×10^{-2} and 7.5×10^{-2} Pa in the main chamber and column, respectively. The sheet resistance of the samples was measured using a low-cost four-point probe.

3. Results and discussion

3.1. Analysis of parameters for irradiation

3.1.1. Influence of Irradiation Number

In the first stage, two samples were prepared using T-80 avocado seed powder under identical laser parameters (10% power, 60 mm s^{-1} scan speed, 4.4 ± 0.2 mm^2 irradiation area) while varying the cooling interval between two irradiation passes. Raman spectra of both samples (Figure 1a) display the characteristic D (~1350 cm^{-1}), G (~1585 cm^{-1}), and 2D (~2700 cm^{-1}) bands associated with graphitic carbon materials. The band positions are consistent with previously reported LIG. [23], [24], [25], [26]

The cooled sample exhibits a lower I_D/I_G ratio compared to the non-cooled sample (Table 2), indicating a reduced defect density in the graphitic lattice when thermal relaxation between irradiations is allowed. The I_{2D}/I_G ratio suggests the presence of multilayered graphene structures in both cases. This result shows that the precursor of avocado Fuerte exhibits a good tendency to graphitize and restructure its aromatic components into a structure commonly reported for LIG green synthesis. [22] Flame retardants are typically used to form an amorphous carbon layer in a first laser pass, then graphitize it in a second pass to form LIG. In contrast, this precursor lacks the flame-retardant treatment and exhibits acceptable graphitization in the first stage of the process. [27]

Optical micrographs (Figure 1b) reveal that two consecutive irradiations compromise the morphological integrity of the pellets, resulting in significant surface roughness and localized ablation. These observations indicate that excessive thermal loading during multiple passes degrades morphological stability without significantly improving graphitization. Consequently, subsequent experiments were conducted using a single irradiation pass. [28]

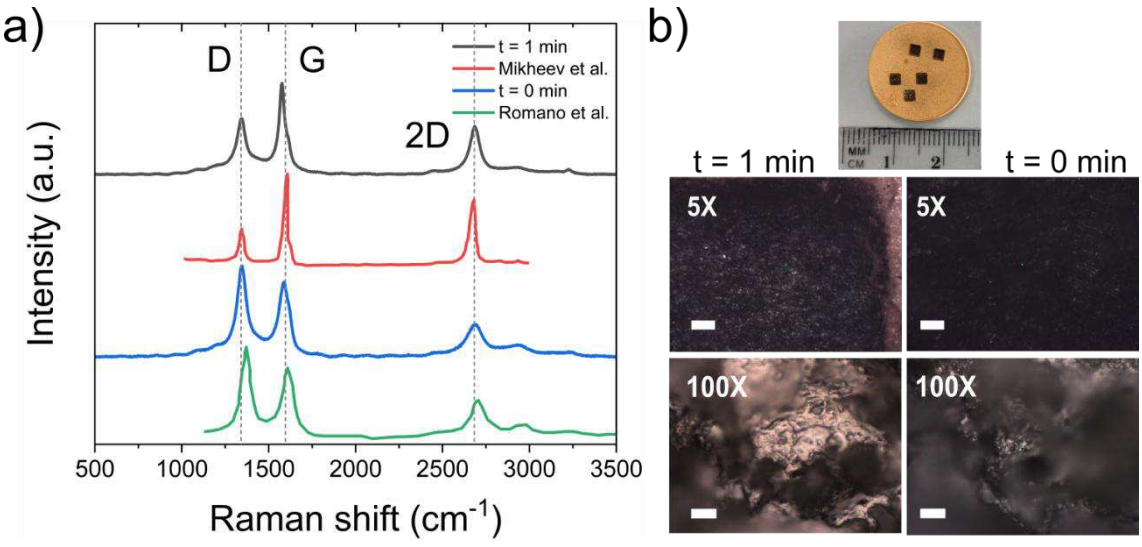


Figure 1. (a) Raman spectra of LIG synthesized under identical laser conditions (10% power, 60 mm s^{-1}, 4 mm^2) with and without a cooling interval between two irradiation passes. (b) Optical micrographs (5×, 20×, 100×) of the irradiated regions showing surface morphology after double-pass irradiation.

Table 2. Raman band intensities and positions (D, G, 2D) for first-stage samples investigating the effect of double-pass irradiation.

Sample	I_{2D}	I_D/I_G	I_{2D}/I_G	D [cm^{-1}]	G [cm^{-1}]	2D [cm^{-1}]
Cooling time	0.53	0.62	0.53	1345.78	1577.57	2687.66
LIG- Mikheev et al.	0.33	0.61	0.33	1364.91	1581.74	2724.69
Without a cooling time	0.36	1.22	0.43	1347.32	1587.30	2688.75
LIG-Romano et al.	0.38	1.33	0.51	1372.44	1609.44	2703.49

3.1.2. Effect of Laser Power and Scan Speed

The effects of laser power and scanning speed on T-80 powder were examined. Although Raman spectra of all samples show multilayer graphene structures reported for LIG (Figure 2a), pellets processed at laser powers (11–12%), area of 4.4 ± 0.2 mm^2, and faster scan speeds exhibited structural degradation and partial material removal. Despite relatively low I_D/I_G ratios in some high-power samples (Table 3), the morphological damage indicates that these conditions approach the ablation threshold of the biomass-derived pellets. The power variation at such low scanning speeds indicates that slight changes in laser power cause material abrasion and damage. Therefore, at low scan speeds, heat accumulates in regions adjacent to the irradiated zone and, when combined with increased laser power, compromises the morphology and structural integrity of the LIG. [29], [30], [31]

The presence of argon flow (Figure 2c) results in a noticeable reduction in D-band intensity, indicating a decrease in defect density in the LIG structure, consistent with previous reports on LIG synthesis under inert atmospheres. The sample processed at 10% laser power, scan speed of 50 mm s^{-1}, and area of 4.4 ± 0.2 mm^2 maintained structural integrity while preserving LIG signatures, indicating a more favorable balance between carbonization and thermal degradation. [31], [32], [33] This condition was therefore selected for further optimization.

Table 3. Raman intensity ratios and band positions for second and third-stage samples synthesized at different laser powers and scan speeds.

Sample		I_D/I_G	I_{2D}/I_G	D	G	2D
Power	Scan Velocity					
[%]	[mm s^{-1}]			[cm^{-1}]	[cm^{-1}]	[cm^{-1}]
10	50	0.175	0.589	1353.16	1585.16	2703.03
11	65	0.059	0.328	1351.18	1585.43	2704.39
12	65	0.285	0.585	1353.72	1585.10	2702.02
10	55	0.65 ± 0.44	0.59 ± 0.08	1352 ± 3	1585 ± 1	2699 ± 6
	50	0.27 ± 0.15	0.54 ± 0.03	1354 ± 1	1586 ± 2	2703 ± 1
	45	0.42 ± 0.22	0.57 ± 0.09	1350 ± 3	1584 ± 2	2699 ± 5
	40	0.75 ± 0.11	0.53 ± 0.09	1352 ± 1	1586 ± 1	2701 ± 2

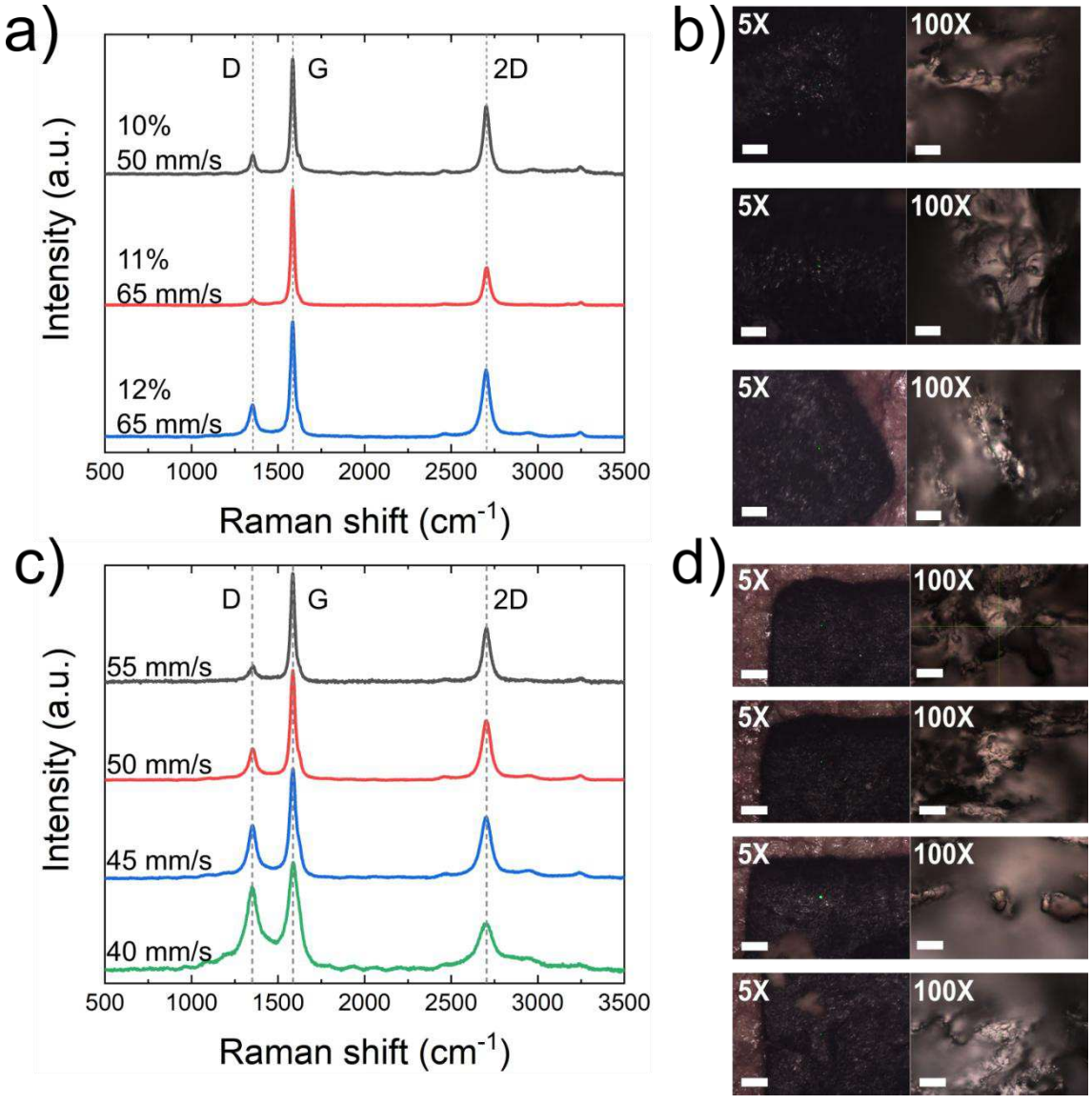


Figure 2. Influence of laser power and scan speed on LIG formation from T-80 avocado seed pellets. (a) Raman spectra of samples processed at different laser powers and scan speeds. (b) Optical micrographs showing morphological degradation at higher laser

powers. (c) Raman spectra of samples synthesized at 10% laser power with varying scan speeds. (d) High-magnification optical micrographs highlighting representative irradiated regions.

3.1.3. Influence of Scan Speed and Processing Flow

A more detailed study of scan speed (S) (40–55 mm s^{-1}) was conducted at 10% laser power and areas of 4.4 ± 0.2 mm^2. Raman analysis at multiple points on each sample (Figure 3a) shows that 50 mm s^{-1} yields the lowest I_D/I_G ratio (0.27 ± 0.15) and the most uniform I_{2D}/I_G ratio (0.54 ± 0.03) values, suggesting reduced defect density and more multilayered graphene structures. All Raman peak ratio results are summarized in Table S1 (Supporting information).

The effect of the atmosphere was then evaluated by comparing the synthesis in ambient air and under argon flow (Figure 3b). Samples processed under argon consistently exhibit lower I_D/I_G ratios, indicating suppression of oxidation and defect formation during laser irradiation. This behavior is consistent with prior reports demonstrating that inert environments favor improved graphitic ordering in LIG by limiting oxygen incorporation and promoting controlled carbonization. [32] All Raman peak ratio results are summarized in Table S2 (Supporting information). Therefore, an argon flow was established as optimal for subsequent experiments.

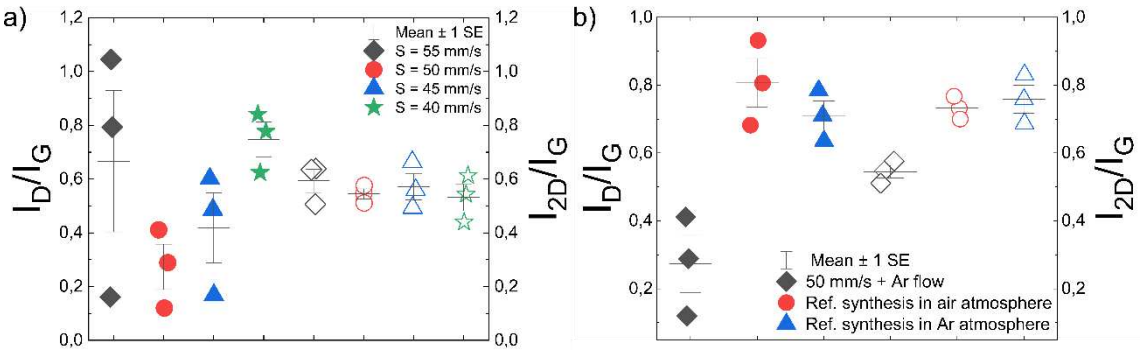


Figure 3. Effect of scan speed and processing atmosphere on the structural quality of LIG. (a) I_D/I_G and I_{2D}/I_G ratios for samples synthesized at different scan speeds (10% laser power, 4 mm^2 area). (b) Comparison of Raman intensity ratios for samples synthesized in ambient air and under argon flow at Reference [32].

3.1.4. Influence of irradiation Area and grain size

The final stage assessed the effect of irradiation area (1.1 ± 0.1, 4.4 ± 0.2, and 9.3 ± 0.2 mm^2) and particle size (T-80, T-140, T-270) under previously optimized conditions (10% power, 50 mm s^{-1}, and argon flow). Raman spectra (Figure 4a) confirm the presence of LIG features across all samples; however, the I_D/I_G ratio increases with decreasing irradiation area from 0.16 ± 0.04 to 0.59 ± 0.30 for T-80 grain size, 0.21 ± 0.08 to 0.72 ± 0.30 for T-140, and 0.27 ± 0.03 to 1.29 ± 0.45 for T-270 (Figure 4b).

Smaller irradiation areas likely produce steeper thermal gradients and lower efficiency in removing volatile species, thereby promoting defect formation and incomplete graphitization. Conversely, larger irradiation areas (9 mm^2) provide more stable thermal conditions and improved outgassing, leading to lower defect densities and better structural ordering. [34]

The I_{2D}/I_G ratio (Figure 4c) with a value of 0.53 ± 0.04 remains below unity for all samples, confirming that the material corresponds to LIG in a multilayer three-dimensional graphene structure rather than monolayer graphene. Analysis of the $I_D/I_{D'}$ ratio (Figure 4d) with a value of 3.1 ± 0.5 indicates that grain boundary–type defects dominate the defect landscape. [34], [35], [36]

Shifts in Raman band positions (Figure 5) further support structural evolution with irradiation area. The gradual redshift of the 2D band in smaller areas suggests increased layer stacking and disorder, consistent with higher defect densities and partial amorphization. [34] All Raman peak ratios and Raman shift results are summarized in Table S3 (Supporting information).

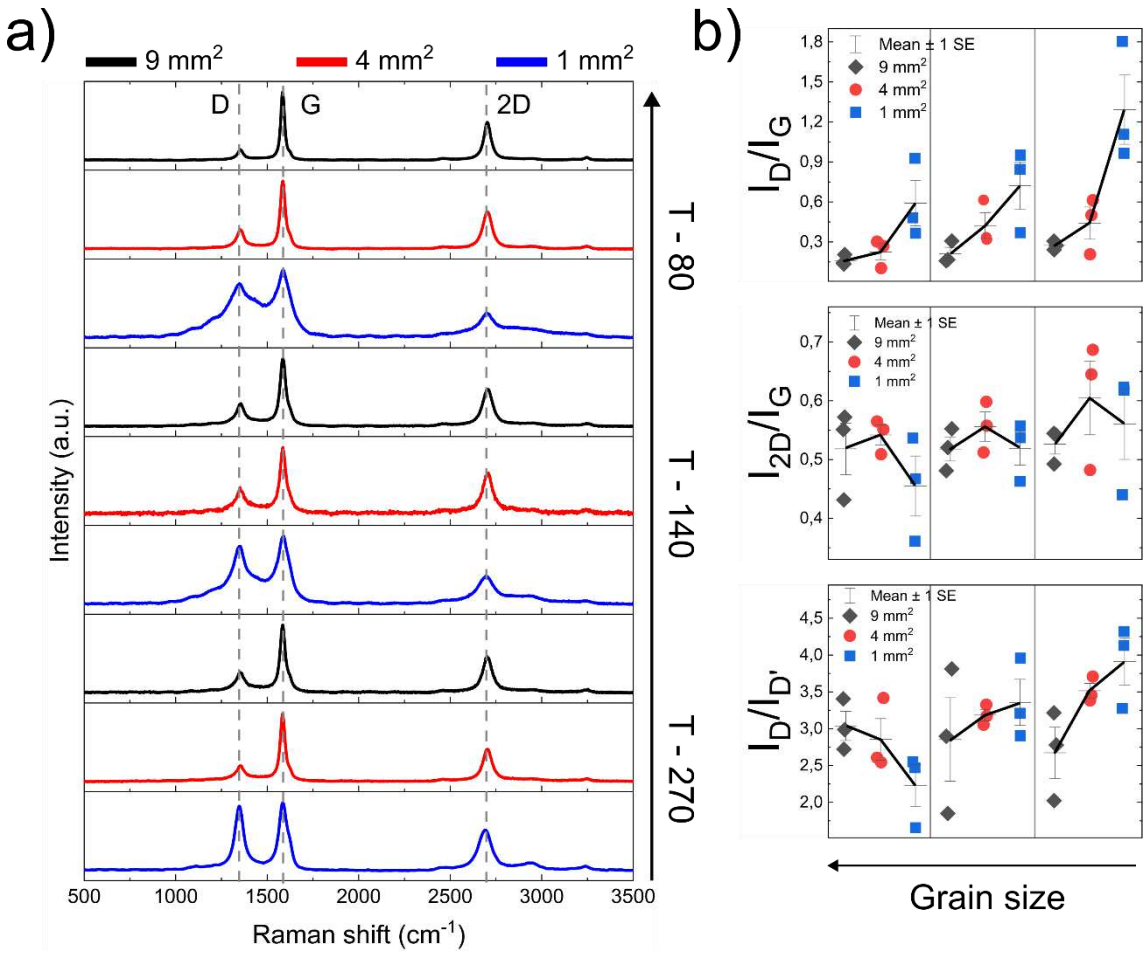


Figure 4. Influence of irradiation area and particle size on LIG structure. (a) Raman spectra of samples synthesized using T-80, T-140, and T-270 powders at irradiation areas of 9, 4, and 1 mm². Evolution of Raman intensity ratios: (b) I_D/I_G, (c) I_{2D}/I_G, and (d) $I_D/I_{D'}$.

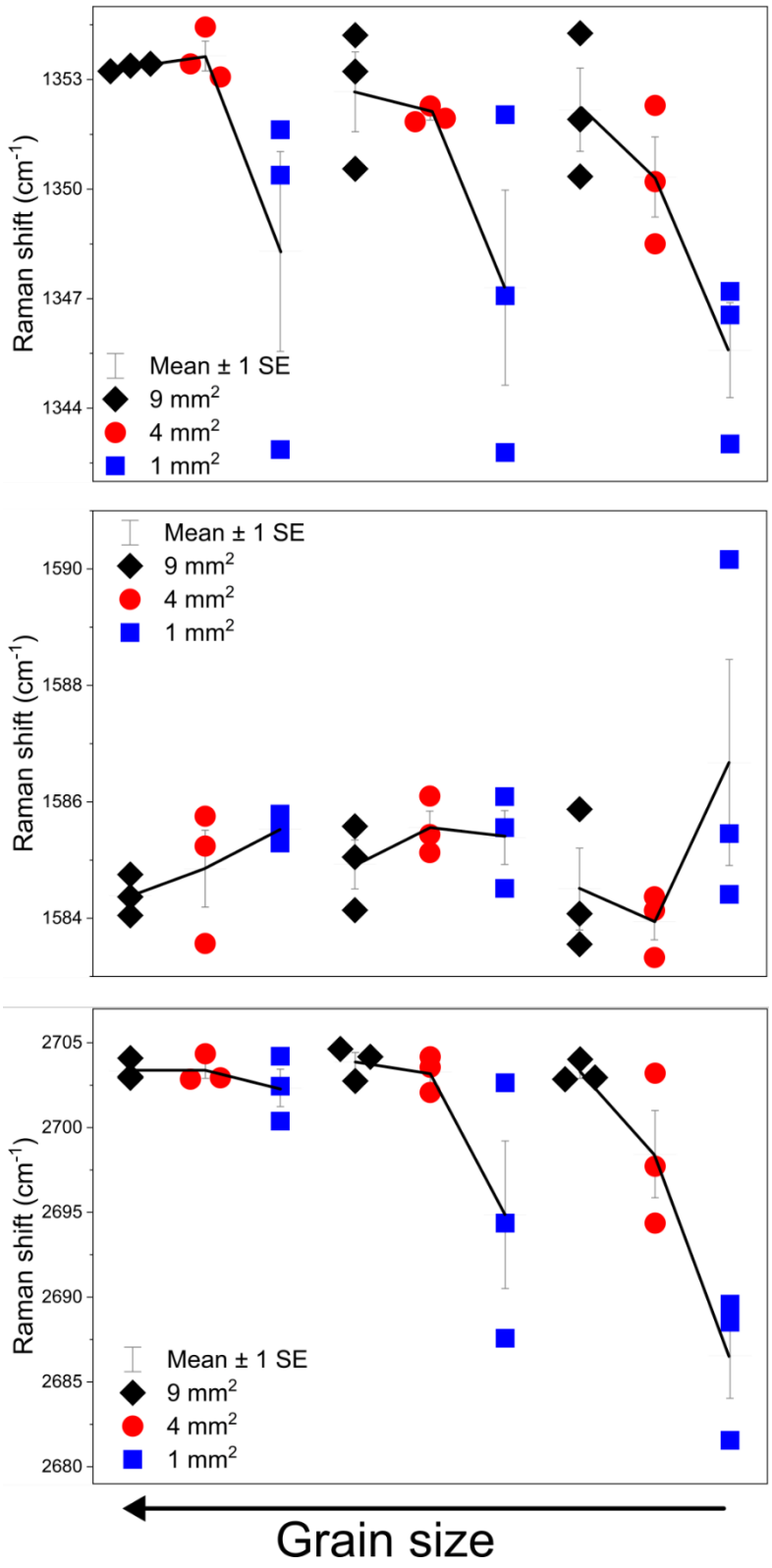


Figure 5. Variation in Raman band positions (D, G, and 2D) as a function of irradiation area and particle size, illustrating structural evolution and changes in graphene layer stacking.

3.1.5. Raman Peak Deconvolution

Detailed deconvolution of the Raman spectra (Figures 6; Tables 4) reveals the presence of characteristic bands in LIG in its conventional positions for the largest and medium areas (9 mm^2 – 4 mm^2). Additional defect-related bands, D*, D_2, and D_4, appear in the smallest-area sample (1 mm^2), confirming significant lattice disorder and hydrogen/oxygen functionalization. [37]

The total sample indicates that decreasing the irradiation area increases the relative contributions of the D, D', and D'' bands, which are associated with hydrocarbon-related structures. Simultaneously, the intensity of the G band decreases in smaller areas, reflecting a reduced fraction of sp^2-bonded carbon. The 2D band slightly decreases, indicating an increase in the number of stacked graphene layers. The D' + D'', D + D', and 2D' bands increase in intensity, indicating an increase in the characteristic double resonance processes of graphene. [36], [37], [38], [39], [40]

The irradiation area is an important factor to consider because, as mentioned, the relationship between power and scanning speed enables uniform heat distribution and improved cooling, so increasing the irradiation area prevents the laser from spending too much time in the same area, thereby reducing damage to the obtained LIG. [30], [31] These findings support the idea that larger irradiation areas promote the formation of LIG with low defect density.

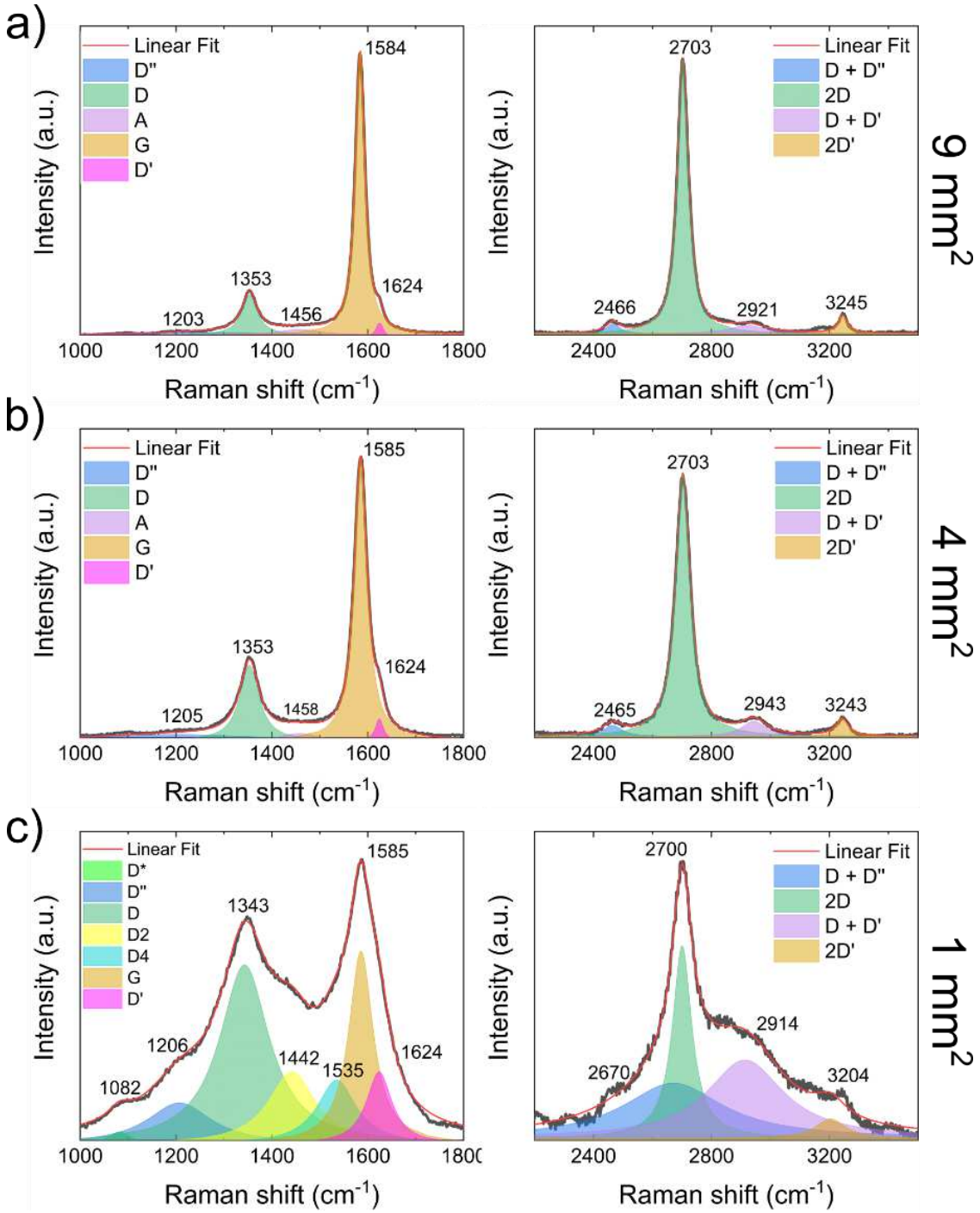


Figure 6. Fitting the Raman spectrum corresponding to samples with an irradiation area of 9 mm^2, 4 mm^2, and 1 mm^2.

Table 4. Raman peak fitting parameters for T-80 samples synthesized at irradiation areas of 9, 4, and 1 mm².

Band		Sample		
		9 mm^2	4 mm^2	1 mm^2
D''	Surface	3.78	15.49	38.34
	Intensity	0.009	0.023	0.149
	FWHM	266.74	426.3	164.19
D	Surface	8.64	20.69	127.10
	Intensity	0.143	0.270	0.640
	FWHM	38.57	48.87	126.36
A	Surface	3.23	2.72	-
	Intensity	0.020	0.027	-
	FWHM	104.25	94.65	-
G	Surface	39.37	52.09	66.98
	Intensity	1.007	1.003	0.690
	FWHM	24.88	33.07	61.83
D'	Surface	0.72	2.48	26.36
	Intensity	0.042	0.079	0.259
	FWHM	16.11	19.92	64.87
D' + D''	Surface	1.74	2.88	46.315
	Intensity	0.021	0.024	0.072
	FWHM	54.15	77.47	412.30
2D	Surface	40.34	52.27	31.22
	Intensity	0.555	0.553	0.249
	FWHM	46.25	60.18	79.70
D + D'	Surface	3.94	5.11	50.56
	Intensity	0.017	0.032	0.102
	FWHM	150.21	100.98	316.58
2D'	Surface	2.24	2.98	4.91
	Intensity	0.036	0.037	0.025
	FWHM	39.42	51.69	124.02

3.1.6. FTIR analysis

FTIR spectra (Figure 7) show that several oxygen-containing functional groups present in the native avocado seed—such as hydroxyl, carbonyl, and ether groups—are partially retained after laser processing (Table 5). According to Ref. 16, avocado seeds are rich in carbon and oxygen, with minor amounts of hydrogen and nitrogen, and contain hemicellulose, cellulose, and lignin, as confirmed by FTIR analysis through characteristic C–O bonds and aromatic ring vibrations at approximately 1020 and 1600 cm^{-1}, respectively. [18] Peaks associated with lignin- and cellulose-derived structures decrease

in intensity but do not disappear entirely, indicating that the process promotes graphitization while preserving residual functional groups. [41] These groups may contribute to surface reactivity and potential application-specific functionality of the LIG.

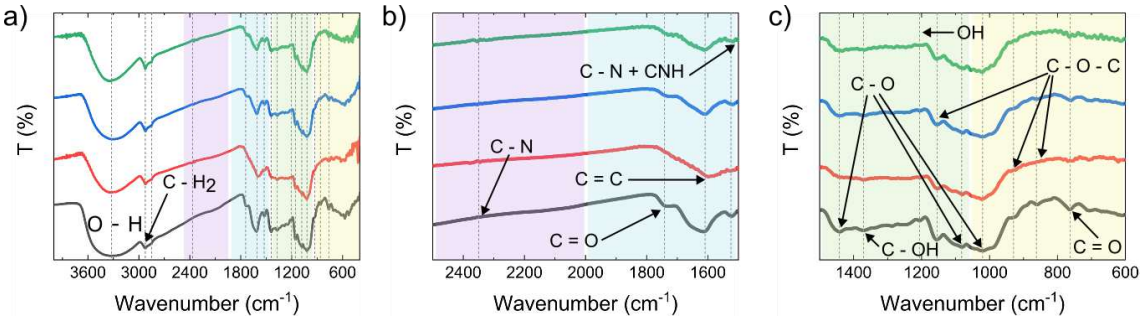


Figure 7. FTIR spectra of untreated avocado seed powder and LIG samples synthesized from T-80 powder with irradiation areas of 9, 4, and 1 mm², showing the evolution of oxygen-containing functional groups after laser processing.

Table 5. FTIR band assignments for avocado seed powder and LIG samples. The nomenclature v, δ, β, v_s y v_{as} represent the vibrational modes stretching, bending, plane deformation, symmetrical stretching, and asymmetric stretching, respectively.

Wavenumber [cm^{-1}]	Chemical bond	Characteristic vibration mode
3323	$v\ O-H$	Water molecules
2925	$v_{as}\ C-H$	Grupo CH_2
2850	$v_s\ C-H$	Grupo CH_2
2367	$v\ C \equiv N$	Nitrile
1746	$v\ C=O$	Ester group ($-COO^-$)
1610	$v\ C=C$	Aromatic ring
1523	$v\ CN\ +\ \delta\ CNH$	Amide group II ($-CO-NH-$)
1415	$v\ C-O$	$-COOH$
1370	$\delta/\beta\ C-OH, C-0H$	Tertiary alcohol group
1205	$v\ O-H$	Phenolic alcohol group
1155	$v\ C-O-C$	Epoxy group
1080	$v\ C-O$	Carboxyl group ($-COOH$) or alkoxy ($-O-$)
1020	$v\ C-O$	$=C-O-C=$
929	Epoxy or peroxide	Epoxy or peroxide
860	$\delta\ C-O-C$	Epoxy group
760	$v\ C=O$	$-COOH$

3.1.7. XPS analysis

XPS measurements provide further evidence of structural evolution as a function of irradiation area (Figure 8, Table 6). The 9 mm² sample (Fig. 8a) exhibits a dominant sp²

carbon peak (~284.8 eV), confirming the successful graphitization of the avocado seed powder. As the irradiated area decreases, sp^3 hybridization appears and oxygen-containing functional groups increase, particularly in the 1 mm^2 sample, where oxidized and hydrogenated species largely replace graphitic carbon. The dominant sp^2 carbon contribution observed in the XPS spectra indicates enhanced graphitic character. However, it does not constitute definitive evidence of crystalline graphene, and is therefore interpreted as indicative of graphitization rather than graphene formation. Interestingly, the 4 mm^2 sample shows a higher apparent sp^2 fraction than the 9 mm^2 sample, suggesting that local chemical composition alone does not fully determine material quality, and must be interpreted alongside defect density and structural integrity. [42], [43], [44] In all samples, two additional functional groups can be identified: epoxy groups, in which oxygen atoms replace carbon atoms within the hexagonal crystal lattice, and carboxylic acid groups, consisting of oxygen and hydroxyl groups attached to the LIG structure. Table 7 shows a comparison of the energy obtained for each chemical species detected in LIG-related studies and the values detected in the samples from this research. The bond energies are close to those reported in other studies on this material. These results align with Raman analysis and demonstrate that larger irradiation areas promote more complete graphitization and reduced chemical disorder.

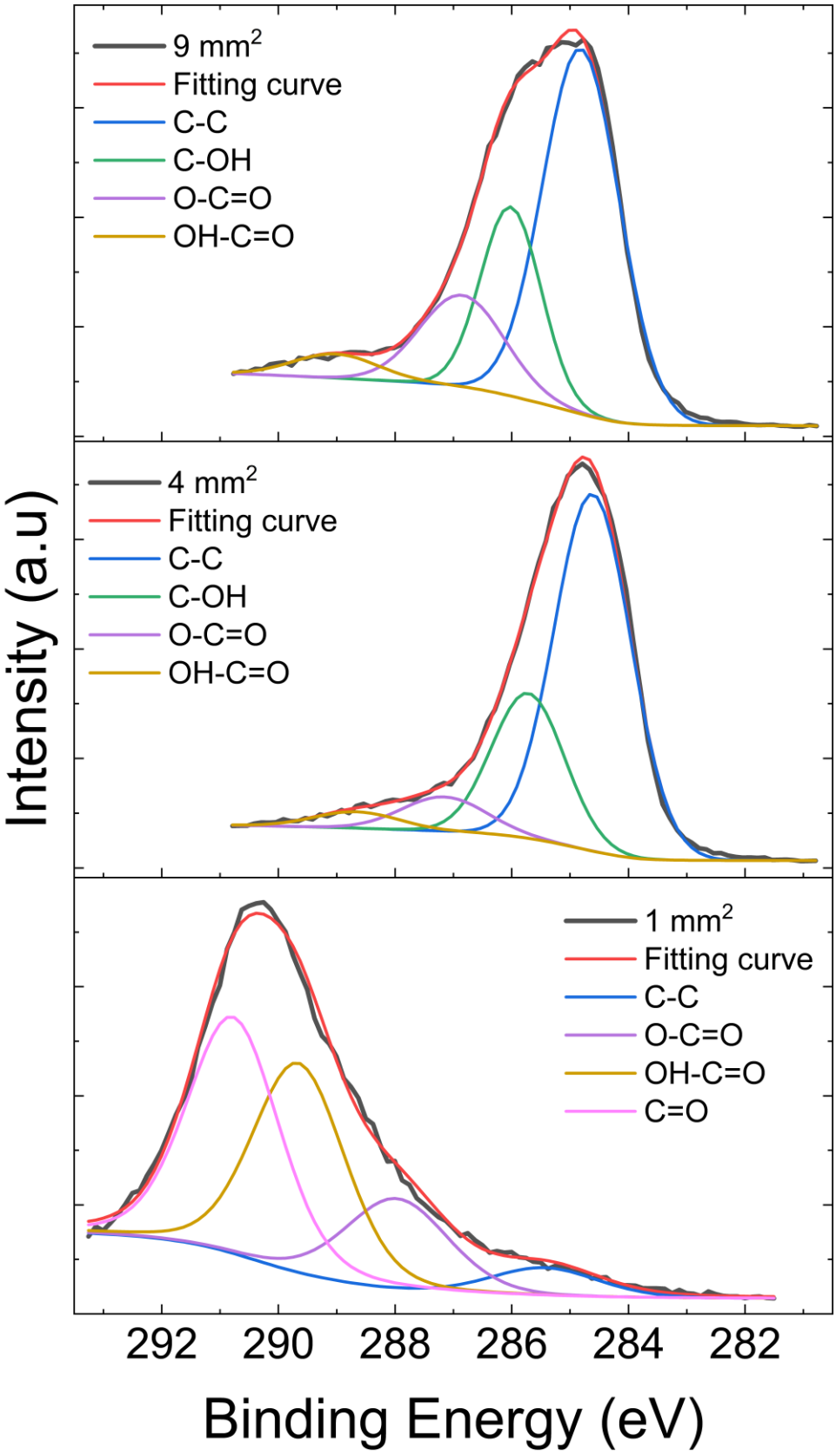


Figure 8. High-resolution C 1s XPS spectra of T-80 samples synthesized at irradiation areas of (a) 9 mm², (b) 4 mm², and (c) 1 mm², illustrating the evolution from dominant sp^2 carbon to increased sp^3 and oxygenated species at smaller irradiation areas.

Table 6. Deconvoluted C 1s XPS peak components and atomic percentages for LIG samples synthesized at different irradiation areas.

Sample	Chemical bond	Bonding energy	FWHM	Intensity	Surface	% Atomic
9 mm²	sp^2	284.81	1.55	2289	2167	57.04
	$C-O$	286.02	1.21	1365	1123	23.14
	$C-O-C$	286.85	1.70	840	544	15.71
	$OH-C=O$	289.02	1.70	496	143	4.12
4 mm²	sp^2	284.61	1.55	1859	3057	64.91
	sp^3	285.72	1.46	755	1175	24.96
	$C=O$	287.16	1.70	179	323	6.86
	$O-C=O$	288.66	1.70	85	154	3.27
1 mm²	sp^3	285.45	2.20	82	211	5.84
	$C=O$	287.97	2.09	257	626	17.35
	$OH-C=O$	289.66	1.86	596	1290	35.74
	$\pi-\pi^*$	290.78	1.85	672	1483	41.07

Table 7. Comparison of C 1s binding energies for LIG samples in this study with reported literature values.

Chemical bond	9 mm²	4 mm²	1 mm²	Binding energy	Reference
sp^2	284.81	284.61	-	284.7- 284.27	[43]
sp^3 / $C-H$	-	285.72	285.45	285.6- 285.32	[42]
$C-O$	286.02	-	-	286.05	[43]
$C-O-C$	286.85	-	-	286.6	[44]
$C=O$	-	287.16	287.97	287.6	[44]
$O-C=O$	-	288.66	-	288.6	[43]
$OH-C=O$	289.02	-	289.66	289.1	[44]
$\pi-\pi^*$	-	-	290.78	290.4	[42]

3.2. Optimal Processing of LIG

The final samples were analyzed using certain synthesis parameters based on considerations derived from the results in section 3.1. Raman spectroscopy (Figure 9a) showed I_D/I_G and I_{2D}/I_G ratios of 0.16 ± 0.07 and 0.48 ± 0.07 cm^{-1}, respectively. All Raman peak ratios and Raman shift results are summarized in Table S4 (Supporting information). These results are consistent with the literature on LIG, which indicates that at laser powers, such as 11%, laser irradiation promotes greater graphitization of the precursor, reducing the presence of amorphous carbon and other carbon-derived structures. [45]

Although the condition at 11% laser power and higher scan speed yields a lower I_D/I_G ratio (0.059), this result must be interpreted with caution. Optical and SEM observations reveal that these conditions approach the ablation threshold of the material, leading to localized degradation and loss of structural integrity. This indicates that the apparent

improvement in Raman metrics arises from selective carbonization rather than uniform graphitization.

Therefore, this condition is considered outside the stable processing window. In contrast, the condition at 10% laser power and 50 mm s^{-1} provides a balance between defect minimization and structural preservation, ensuring reproducible material formation. Consequently, the optimal condition is defined not by the absolute minimum I_D/I_G value, but by the intersection of the low-defect-density and structural-stability constraints.

The morphology of LIG revealed a porous layer with a high concentration of hierarchical structures. Image analysis shows a pore size of 1.2 ± 0.8 μm in certain areas of the sample (light blue box), as well as pore sizes of 1.15 ± 0.39 and 2.11 ± 1.24 μm in the green and yellow areas, respectively. The formation of pores of varying sizes is due to the release of gases from the material's graphitization. [46] Finally, the sheet resistance of these samples was 25.31 ± 1.09 Ω sq^{-1}, a value that is indeed high compared with those expected in lignocellulosic materials, yet still represents greater efficiency than other aliphatic precursors that require fire retardants to improve their graphitization quality and electrical characteristics. [22]

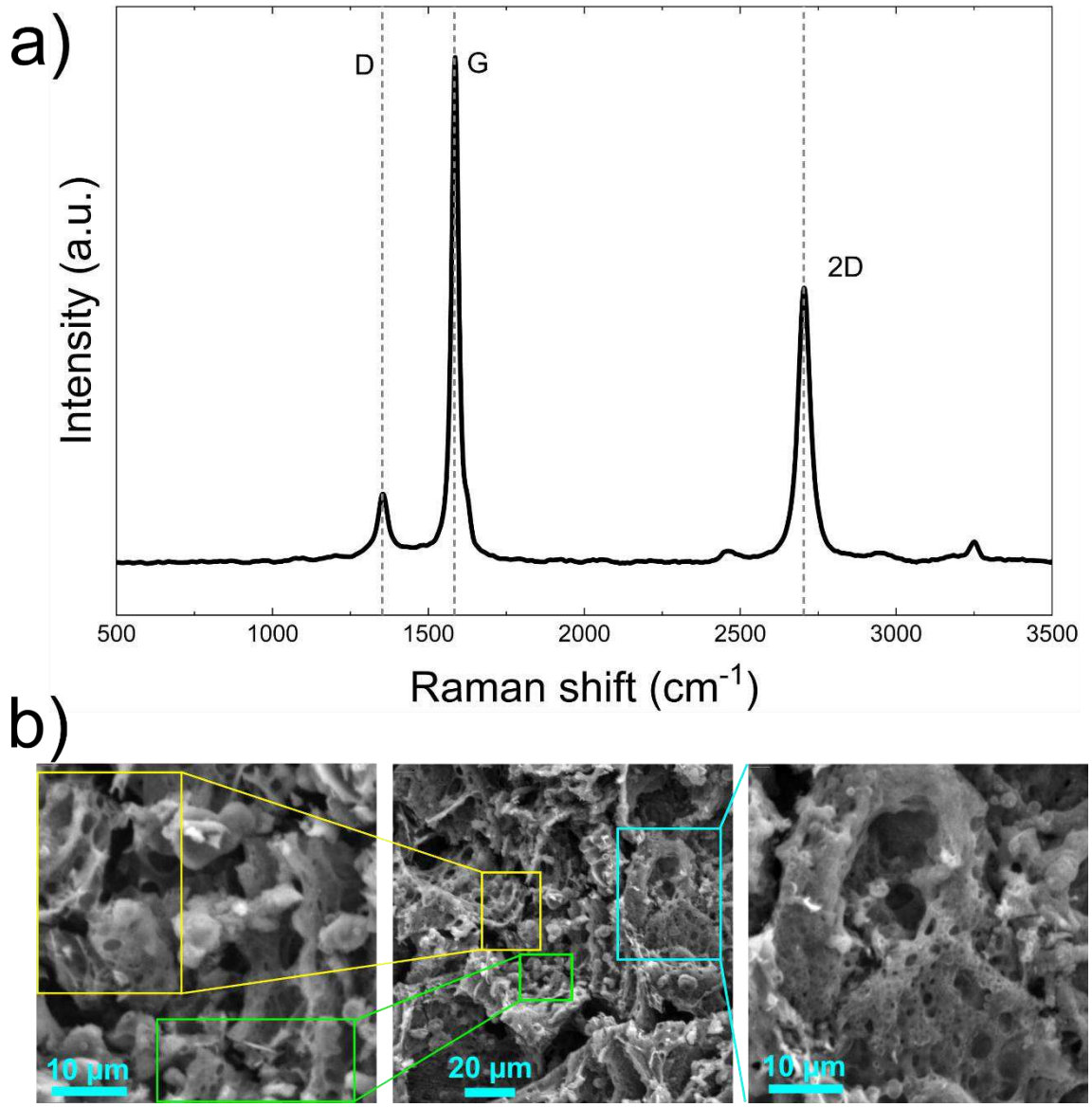


Figure 9. LIG was synthesized with a laser power of 11%, at 50 mm s^{-1} with a defocus distance of 9 mm. (a) Ramana spectrum of a representative sample of the LIG synthesis. (b) SEM images (1000×) of the irradiated regions showing surface morphology.

Discussion on Optimal Processing Parameters

The determination of optimal laser processing conditions in biomass-derived systems cannot rely on a single parameter, such as the Raman I_D/I_G ratio alone. Although this metric provides a useful indication of defect density, it does not account for the material's physical stability under laser irradiation.

In this work, the optimization is reformulated as a multi-criteria process window, defined by the simultaneous fulfillment of three conditions: i) Minimization of defect density (low

I_D/I_G ratio), ii) Preservation of structural integrity (absence of ablation or collapse), and iii) Process stability (reproducibility across multiple regions and samples). This approach allows distinguishing between conditions that are spectroscopically favorable but physically unstable, and those that are both structurally and functionally viable.

4. Conclusion

This study demonstrates that optimal conditions in biomass-derived systems are governed not by a single spectroscopic parameter, but by the intersection of defect minimization and thermomechanical stability, defining a physically meaningful processing window. Through systematic optimization of processing parameters, including laser power, scan speed, irradiation area, and argon flow in the synthesis, the conditions required to obtain higher-quality graphitic structures from biomass-derived pellets were identified.

Raman spectroscopy revealed that LIG synthesized with a T-80 grain size at 10% laser power, a scan speed of 50 mm s^{-1}, single-pass irradiation, and argon flow exhibited the lowest defect density. The irradiation area was found to be a critical factor governing structural quality: larger areas promoted more uniform thermal distribution, improved removal of volatile species, and enhanced graphitic ordering, while smaller areas led to increased disorder and amorphous carbon formation. This is demonstrated by the lower I_D/I_G ratio of 0.16 ± 0.04 for the 9 mm^2 area. Deconvolution of Raman spectra confirmed that defect-related bands intensified as the irradiated region decreased, supporting this interpretation.

FTIR analysis showed that although laser processing drives extensive carbonization, oxygen-containing functional groups originating from lignocellulosic components are partially retained, yielding a functionalized three-dimensional graphene network as evidenced by bands at 1020 and 1600 cm^{-1}. XPS results further confirmed the predominance of sp^2-hybridized carbon under optimized conditions, while smaller irradiation areas showed increased sp^3 carbon and oxygenated species, indicating incomplete graphitization.

Analysis of the LIG with a large area of 56.4 ± 3 mm^2 showed a low defect density, as expected given its low I_D/I_G ratio of 0.16 ± 0.07 cm^{-1} and porous morphology, typical for this type of material. The sheet strength was 25.31 ± 1.09 Ω sq^{-1}, which, although relatively high for this material, is noteworthy due to the ease of processing of the

precursor material and the absence of a flame retardant, which is commonly used for optimal LIG synthesis.

The main contribution of this work lies not only in demonstrating the feasibility of producing laser-induced graphitic carbon from avocado seed biomass, but in establishing a reproducible multi-parameter processing framework for lignocellulosic precursors. The identification of a stable processing window—defined by the balance between defect density and structural integrity—represents a key step toward scalable and reliable fabrication. Furthermore, achieving graphitization without flame retardants addresses a major limitation in biomass-derived systems. These findings provide a foundation for extending laser-induced synthesis of graphitic materials to a broader class of sustainable carbon sources.

5. Declarations

5.1. Ethical Approval

Not applicable.

5.2. Funding

Not applicable.

5.3. Availability of data and materials

Not applicable.

6. Reference

1. Si, C., Sun, Z. & Liu, F. Strain engineering of graphene: a review. *Nanoscale* **8**, 3207–3217 (2016).
2. Lü, K., Zhao, G. X. & Wang, X. K. A brief review of graphene-based material synthesis and its application in environmental pollution management. *Chinese Science Bulletin* **57**, 1223–1234 (2012).
3. Jiang, L. & Fan, Z. Design of advanced porous graphene materials: from graphene nanomesh to 3D architectures. *Nanoscale* **6**, 1922–1945 (2014).
4. Sun, Z., Fang, S. & Hu, Y. H. 3D Graphene Materials: From Understanding to Design and Synthesis Control. *Chem. Rev.* **120**, 10336–10453 (2020).
5. Ye, R., James, D. K. & Tour, J. M. Laser-Induced Graphene: From Discovery to Translation. *Advanced Materials* **31**, 1803621 (2019).

6. Pinheiro, T. *et al.* Direct Laser Writing: From Materials Synthesis and Conversion to Electronic Device Processing. *Advanced Materials* **36**, 2402014 (2024).

7. Le, T. S. D. *et al.* Recent Advances in Laser-Induced Graphene: Mechanism, Fabrication, Properties, and Applications in Flexible Electronics. *Adv. Funct. Mater.* **32**, 2205158 (2022).

8. Vivaldi, F. M. *et al.* Three-Dimensional (3D) Laser-Induced Graphene: Structure, Properties, and Application to Chemical Sensing. *ACS Appl. Mater. Interfaces* **13**, 30245–30260 (2021).

9. Li, G. Direct laser writing of graphene electrodes. *J. Appl. Phys.* **127**, 010901 (2020).

10. Lin, J. *et al.* Laser-induced porous graphene films from commercial polymers. *Nature Communications 2014 5:1* **5**, 1–8 (2014).

11. Chyan, Y. *et al.* Laser-Induced Graphene by Multiple Lasing: Toward Electronics on Cloth, Paper, and Food. *ACS Nano* **12**, 2176–2183 (2018).

12. Yu, Q., Jiang, J., Jiang, L., Yang, Q. & Yan, N. Advances in green synthesis and applications of graphene. *Nano Research 2021 14:11* **14**, 3724–3743 (2021).

13. Santos, F. A. & Correa, D. S. Turning Waste into Sensors: Sustainable Pesticide Detection Using Orange Peel-Derived Laser-Induced Graphene. *ACS Omega* **10**, 49126–49135 (2025).

14. Steksova, Y. *et al.* Laser-Induced Graphene from Waste Almond Shells. *Adv. Funct. Mater.* e07462 (2025) doi:10.1002/ADFM.202507462;WGROUP:STRING:PUBLICATION.

15. Yang, Q. *et al.* Upgrading pomelo peels into laser-induced graphene for multifunctional sensors. *J. Anal. Appl. Pyrolysis* **173**, 106074 (2023).

16. Min, J., Ko, S. H., Jung, Y. & Lee, J. Laser-induced graphene based on paper for smart food decay sensor. *https://doi.org/10.1117/12.2644667* **12409**, 211–216 (2023).

17. INIAP evalúa cultivo de aguacate – Ministerio de Agricultura y Ganadería. https://www.agricultura.gob.ec/iniap-evalua-cultivo-de-aguacate/.

18. Durak, H. & Aysu, T. Effect of pyrolysis temperature and catalyst on production of bio-oil and bio-char from avocado seeds. *Research on Chemical Intermediates* **41**, 8067–8097 (2015).

19. Nyakang'I, C. O., Marete, E., Ebere, R. & Arimi, J. M. Physicochemical Properties of Avocado Seed Extract Model Beverages and Baked Products Incorporated with Avocado Seed Powder. *Int. J. Food Sci.* **2023**, (2023).

20. Pinheiro, T. *et al.* Influence of CO2 laser beam modelling on electronic and electrochemical properties of paper-based laser-induced graphene for disposable pH electrochemical sensors. *Carbon Trends* **11**, 100271 (2023).

21. Ghanam, A. *et al.* Lignin-derived laser-induced graphene: toward a green and scalable route for energy and environmental applications. *Green Chemistry* https://doi.org/10.1039/d5gc05595d (2026) doi:10.1039/d5gc05595d.

22. Pedro, P. I. *et al.* Sustainable carbon sources for green laser-induced graphene: A perspective on fundamental principles, applications, and challenges. *Appl. Phys. Rev.* **9**, (2022).

23. Mikheev, K. G., Zonov, R. G., Bulatov, D. L., Fateev, A. E. & Mikheev, G. M. Laser-Induced Graphene on a Polyimide Film: Observation of the Photon Drag Effect. *Technical Physics Letters 2020 46:5* **46**, 458–461 (2020).

24. Romano, V., Torrisi, L., Cutroneo, M., Havranek, V. & D'Angelo, G. Raman investigation of laser-induced structural defects of graphite oxide films. *EPJ Web Conf.* **167**, 04011 (2018).

25. Wahab, H. *et al.* Machine-learning-assisted fabrication: Bayesian optimization of laser-induced graphene patterning using in-situ Raman analysis. *Carbon N. Y.* **167**, 609–619 (2020).

26. Zhu, J., Guo, X., Wang, H. & Song, W. Cost-effective fabrication and high-frequency response of non-ideal RC application based on 3D porous laser-induced graphene. *J. Mater. Sci.* **53**, 12413–12420 (2018).

27. Chyan, Y. *et al.* Laser-Induced Graphene by Multiple Lasing: Toward Electronics on Cloth, Paper, and Food. *ACS Nano* **12**, 2176–2183 (2018).

28. Nasser, J., Lin, J., Zhang, L. & Sodano, H. A. Laser induced graphene printing of spatially controlled super-hydrophobic/hydrophilic surfaces. *Carbon N. Y.* **162**, 570–578 (2020).

29. Bokobza, L., Bruneel, J.-L., Couzi, M. & Thakur, V. K. Raman Spectra of Carbon-Based Materials (from Graphite to Carbon Black) and of Some Silicone Composites. *C 2015, Vol. 1, Pages 77-94* **1**, 77–94 (2015).

30. Moon, H. R. & Ryu, B. Review of Laser-Induced Graphene (LIG) Produced on Eco-Friendly Substrates. *International Journal of Precision Engineering and Manufacturing-Green Technology 2024 11:4* **11**, 1279–1294 (2024).

31. Silvestre, S. L. *et al.* Cork derived laser-induced graphene for sustainable green electronics. *Flexible and Printed Electronics* **7**, 035021 (2022).

32. Li, Y. *et al.* Laser-Induced Graphene in Controlled Atmospheres: From Superhydrophilic to Superhydrophobic Surfaces. *Advanced Materials* **29**, 1700496 (2017).

33. Trusovas, R., Račiukaitis, G., Barkauskas, J. & Mažeikienė, R. Laser Induced Graphite Oxide/Graphene Transformation. *JLMN-Journal of Laser Micro/Nanoengineering* **7**, (2012).

34. Murray, R., Burke, M., Iacopino, D. & Quinn, A. J. Design of Experiments and Optimization of Laser-Induced Graphene. *ACS Omega* **6**, 16736–16743 (2021).

35. Dathbun, A. & Chaisitsak, S. Effects of three parameters on graphene synthesis by chemical vapor deposition. *8th Annual IEEE International Conference on Nano/Micro Engineered and Molecular Systems, IEEE NEMS 2013* 1018–1021 (2013) doi:10.1109/NEMS.2013.6559895.

36. Merlen, A., Buijnsters, J. G. & Pardanaud, C. A Guide to and Review of the Use of Multiwavelength Raman Spectroscopy for Characterizing Defective Aromatic Carbon Solids: from Graphene to Amorphous Carbons. *Coatings 2017, Vol. 7, Page 153* **7**, 153 (2017).

37. Liang, Q., Yao, X., Wang, W., Liu, Y. & Wong, C. P. A Three-Dimensional Vertically Aligned Functionalized Multilayer Graphene Architecture: An Approach for Graphene-Based Thermal Interfacial Materials. *ACS Nano* **5**, 2392–2401 (2011).

38. Ghavipanjeh, A. & Sadeghzadeh, S. Simulation and experimental evaluation of laser-induced graphene on the cellulose and lignin substrates. *Scientific Reports 2024 14:1* **14**, 1–13 (2024).

39. Herziger, F., Mirzayev, R., Poliani, E. & Maultzsch, J. In-situ Raman study of laser-induced graphene oxidation. *physica status solidi (b)* **252**, 2451–2455 (2015).

40. Santos, N. F. *et al.* IR and UV Laser-Induced Graphene: Application as Dopamine Electrochemical Sensors. *Adv. Mater. Technol.* **6**, 2100007 (2021).

41. Ye, R. *et al.* Laser-Induced Graphene Formation on Wood. *Advanced Materials* **29**, 1702211 (2017).

42. Kulyk, B. *et al.* Laser-Induced Graphene from Paper for Mechanical Sensing. *ACS Appl. Mater. Interfaces* **13**, 10210–10221 (2021).

43. Coelho, J. *et al.* Paper-based laser-induced graphene for sustainable and flexible microsupercapacitor applications. *Microchimica Acta* **190**, (2023).

44. Shi, Q., Hou, C., Wang, H., Zhang, Q. & Li, Y. Rapid formation of superelastic 3D reduced graphene oxide networks with simultaneous removal of HI utilizing NIR irradiation. *J. Mater. Chem. A Mater.* **3**, 9882–9889 (2015).

45. Qu, W. *et al.* Direct laser writing of pure lignin on carbon cloth for highly flexible supercapacitors with enhanced areal capacitance. *Sustain. Energy Fuels* **5**, 3744–3754 (2021).

46. Mahmood, F., Mahmood, F., Zhang, H., Lin, J. & Wan, C. Laser-Induced Graphene Derived from Kraft Lignin for Flexible Supercapacitors. *ACS Omega* **5**, 14611–14618 (2020).

Supplementary Files

This is a list of supplementary files associated with this preprint. Click to download.

- Supplementaryfile1.pdf